Scintillation efficiency and ionization yield of liquid xenon for mono-energetic nuclear recoils down to 4 keV

A. Manzur,[1] A. Curioni,[1, *] L. Kastens,[1] D.N. McKinsey,[1, †] K. Ni,[1, ‡] and T. Wongjirad[1, §]

[1]Department of Physics, Yale University, P.O. Box 208120, New Haven, CT 06520, USA

(Dated: January 18, 2010)

Liquid Xenon (LXe) is an excellent material for experiments designed to detect dark matter in the form of Weakly Interacting Massive Particles (WIMPs). A low energy detection threshold is essential for a sensitive WIMP search. The understanding of the relative scintillation efficiency ($\mathcal{L}_{\text{eff}}$) and ionization yield of low energy nuclear recoils in LXe is limited for energies below 10 keV. In this paper, we present new measurements that extend the energy down to 4 keV, finding that $\mathcal{L}_{\text{eff}}$ decreases with decreasing energy. We also measure the quenching of scintillation efficiency due to the electric field in LXe, finding no significant field dependence.

PACS numbers: 95.35.+d, 29.40.Mc, 95.55.Vj

I. INTRODUCTION

Liquid xenon is increasingly used as the detection material in direct searches for WIMP dark matter [1]. Recent developments in two-phase (gas/liquid) xenon detectors [2–4] has resulted in stringent limits on the WIMP-nucleon cross-section, constraining theories of physics beyond the standard model, such as supersymmetry. WIMPs will deposit a small amount of energy in the LXe through elastic scatters with xenon nuclei. Part of the deposited energy is converted into observable signals of scintillation light and ionization electrons. The rest of the energy is converted into heat and can not be easily measured. Understanding these effects will help determine nuclear recoil energies and ultimately play a part in determining the WIMP-nucleon cross-section.

In a two-phase xenon detector, two signals are measured. The first is the direct scintillation light, denoted as $S1$. The second is the proportional scintillation light in the gas phase, denoted as $S2$, which is proportional to the ionization electrons that survive electron-ion recombination and are extracted into the gas. Figure 1 gives an illustration of the signal production and collection in a two-phase xenon detector.

For a given event in the LXe, the nuclear recoil energy can be determined based on the scintillation signal $S1$ [2, 3]. However, it is much more convenient to calibrate the detector using electron recoil events. The tradition in the field [5–9] is to base the energy calibration on 122 keV electron recoils from a ^{57}Co gamma source. The *relative scintillation efficiency*, $\mathcal{L}_{\text{eff}}$, defined as the ratio between the electron equivalent energy (E_{ee}) and the true nuclear recoil energy (E_r), becomes necessary for determining the nuclear energy scale and, therefore, the WIMP detection sensitivity. E_{ee} is inferred from the scintillation signal yield due to monoenergetic electron recoils. $\mathcal{L}_{\text{eff}}$ has no units and is defined at zero electric field in LXe relative to 122 keV gamma rays.

If an electric field is applied to the LXe, the scintillation yields for both electron and nuclear recoils are suppressed by additional factors S_e and S_n, respectively. The relative scintillation efficiency can be calculated as

$$\mathcal{L}_{\text{eff}} = E_{ee}/E_r \cdot S_e/S_n \qquad (1)$$

The quantity S_e for 122 keV electron recoils from a ^{57}Co source has been measured very accurately [10]. S_n has been measured for 56 keV nuclear recoils, with electric fields up to a few kV/cm in LXe [7, 10], but no measurement is available for nuclear recoils at other energies.
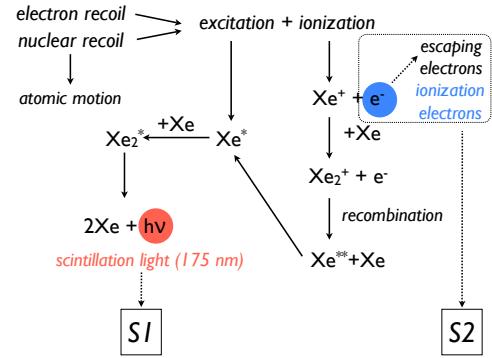

FIG. 1: (Color online) Illustration of the signal production and collection in a two-phase xenon detector.

Two methods have been utilized to determine $\mathcal{L}_{\text{eff}}$ as a function of energy: a) Using a fixed-energy neutron beam experiment, detecting neutrons that scatter in the LXe at a known scattering angle, and b) Comparing neutron calibration data to Monte Carlo simulations without

tagging the scattered neutron. Using method a), $\mathcal{L}_{eff}$ has been measured by a number of groups for nuclear recoils above 10 keV [5–7]. There are also two measurements of this type reporting results below 10 keV, one suggesting an increasing $\mathcal{L}_{eff}$ with decreasing energies [8], and another indicating a roughly constant $\mathcal{L}_{eff}$ of 0.15 down to 5 keV [9]. The XENON10 and the ZEPLIN-III collaborations have also determined $\mathcal{L}_{eff}$ with method b) [4, 11, 12]. In the XENON10 analysis, $\mathcal{L}_{eff}$ does not decrease much at low energies, while in the ZEPLIN-III measurement, the data imply a precipitous drop at low energies.

In this paper, we report on measurements of $\mathcal{L}_{eff}$ at zero field and S_n at two different fields (0.73 kV/cm and 1.5 kV/cm) for nuclear recoils between 4 and 66 keV in a single phase detector ($S1$-only). We repeated these measurements using a dual phase detector ($S1$ and $S2$ signals) at 1 kV/cm in the liquid and 10 kV/cm in the gas as well as 4 kV/cm in the liquid and 8 kV/cm in the gas. With the dual phase detector we also measured the ionization signal yield for nuclear recoils. We present the experimental apparatus in Section II, the data analysis in Section III, the results in Section IV, a theoretical model of $\mathcal{L}_{eff}$ in Section V and a discussion of the results in Section VI.

II. EXPERIMENTAL APPARATUS

The measurement was performed with a setup comprising a deuterium-deuterium neutron generator [13], a LXe detector, and an organic liquid scintillator detector, as shown in Figure 2. The neutron generator produces 2.8 MeV neutrons at a rate of 10^6 n/s. The liquid scintillator detector is a BC501A organic scintillator module 3.8 cm in diameter and 3.8 cm in height, viewed by a photomultiplier (PMT). Both the neutron generator and the organic scintillator detector have previously been used to perform measurements of nuclear recoils in liquid argon [14] and liquid neon [15]. The LXe detector is made of a cylinder of LXe viewed by two Hamamatsu R9869 PMTs, as shown in Figure 3. The PMTs are specially designed for LXe applications. They have a bialkali photo-cathode and a quartz window with an aluminum strip pattern on the photo-cathode. The two PMTs have a quantum efficiency of 36% for LXe scintillation light at 175 nm. The collection efficiency from the photo-cathode to the first dynode is about 70%. The active LXe target is 5 cm in diameter and 2 cm in height and is surrounded by polytetrafluoroethylene (PTFE) for UV light reflection. The thickness of the PTFE is minimized (11.5 mm) to reduce neutron multiple scatters with surrounding materials. Two stainless steel mesh grids, each with 90% optical transparency, are installed to apply electric field to the LXe. In dual phase mode, a third grid is added to apply a separate electric field in the xenon gas region.

The LXe detector is located in an aluminum vacuum cryostat and cooled by a pulse-tube refrigerator (PTR). The cryogenic system is described else-

where [16]. The neutron generator is shielded by 30.5 cm × 30.5 cm × 30.5 cm water boxes and two 10 cm × 30 cm × 30 cm polyethylene slabs to block and absorb neutrons that are emitted in directions other than toward the cryostat. The distance from the neutron generator to the center of the LXe was 76 cm. The distance between the center of the LXe and the center of the organic scintillator varied from 16 to 20 cm between runs. The scattering angle, defined by the position of the organic scintillator (Figure 2), was varied from 25 to 125 degrees to vary the associated recoil energy.
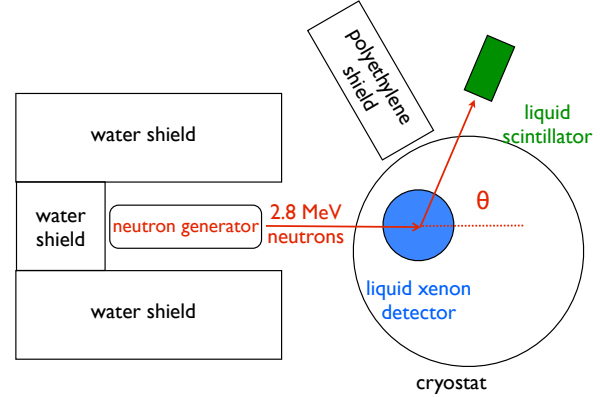

FIG. 2: (Color online) The setup for nuclear recoil scintillation efficiency measurement in LXe. Not drawn to scale.
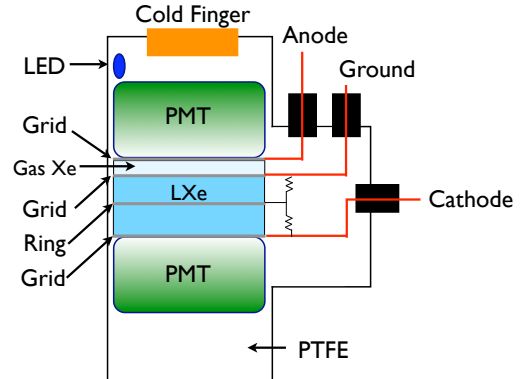

FIG. 3: (Color online) Schematic of the dual phase LXe detector. Spaces not drawn were filled with PTFE pieces. PMTs, LXe and xenon gas regions drawn to scale.

During the single phase runs, the PMT waveforms were recorded with an 8-bit oscilloscope, model TDS-5034B from Tektronix. The oscilloscope's logic gate was used to trigger the data acquisition system, triggering on triple coincidence (both $S1$ signals and the organic scintillator signal) in a 80 ns window.

For the dual phase runs, a VME 12-bit, 250 MS/s digitizer (CAEN V1720) was used, because of its higher dynamic range. An external trigger for the VME digitizer was generated using external NIM modules. In this mode the data acquisition system was triggered by the $S2$ signals. At a few scattering angles, data acquisition was instead triggered by the $S1$ signals to test for any systematic effects due to the trigger. For the $S2$ trigger, shown in Figure 4, the PMT signals were added and integrated using a FAN IN/OUT and an integrator module. The summed and integrated signal then went to a discriminator to select the $S2$ signals. The scintillator signal was sent through a discriminator to avoid small pulses. The output signal was used to generate a 15 μs pulse with the help of a gate generator. This pulse in coincidence with the $S2$ pulse generated the trigger for the acquisition system. For the $S1$ trigger we reproduced the trigger system described above for single phase operation, but using NIM modules. In both the single and dual phase runs, the data were recorded at a rate of ~5 Hz.
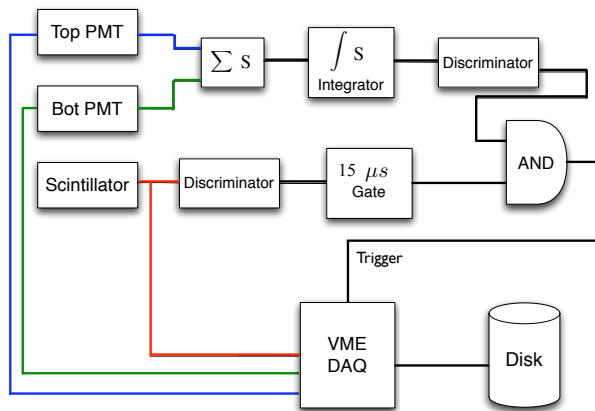

FIG. 4: (Color online) Trigger system used in the dual phase runs. The PMT signals are summed and integrated to select the $S2$ signals. The organic scintillator signal generates a 15 μs pulse. This pulse and the $S2$ signals in coincidence trigger the acquisition system. For the single phase runs, triple coincidence of the $S1$ signals and the organic scintillator signal triggers the acquisition system.

Throughout the runs, periodic calibrations were performed to test the stability of the PMTs and measure the purity of the LXe. The gains of the two PMTs were measured from the single photoelectron (pe) spectra by using light emitted from a blue LED located inside the LXe detector. The energy scale is calibrated using 122 keV gamma rays from a ^{57}Co source located outside the cryostat. The scintillation signal yields for the 122 keV gamma rays in LXe in the single phase detector are 10.8 ± 0.1 pe/keVee (keV in electron equivalent) at zero field and 4.8 ± 0.1 pe/keVee at 1.5 kV/cm (Figure 5). After adding a third grid and PTFE spacer and then removing some LXe to run the dual phase mode,

the light yield drops to 9.5 ± 0.2 pe/keVee at zero field and 4.3 ± 0.1 pe/keVee at 1.0 kV/cm drift field. The light yields from the 122 keV events were monitored over the entire period of the measurements finding an additional fluctuation less than 3%.
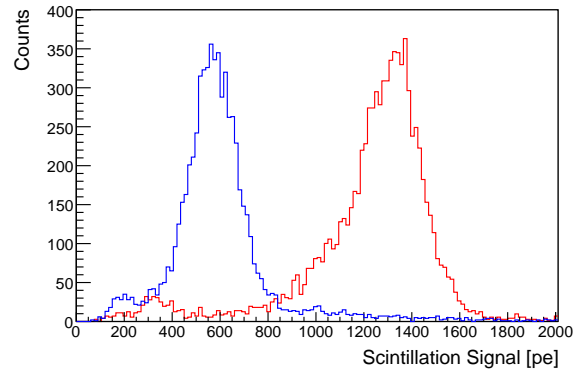

FIG. 5: (Color online) Scintillation light yield for 122 keV gamma rays in the LXe detector running in single phase. The left histogram was taken at 1.5 kV/cm yielding 4.8±0.1 pe/keVee and a resolution (σ/E) of 18%. The right histogram was taken at 0.0 kV/cm yielding 10.8 ± 0.1 pe/keVee and a resolution of 8.8%.

During the single phase runs, the LXe purity was monitored by measuring the stability of the scintillation signal yield from 122 keV gamma rays. During the dual phase runs, the purity was also monitored by measuring the electron lifetime, τ, found by fitting the $S2$ spectrum with $S2 = S2_0 \exp\left[-dt/\tau\right]$ where dt is the electron drift time, measured as the time between the $S1$ and $S2$ signals. For the data presented here, electron lifetime was greater than 40 μs and continuously improved over the course of the experiment. By the end of the experiment, the electron lifetime was 90 μs. The total drift time for events at the cathode grid is 12 μs. The $S2$ signals were corrected for the electron lifetime. Figure 6 shows a typical $S2$ spectrum for 122 keV gamma rays taken during the dual phase runs.

III. FINDING $\mathcal{L}_{\mathrm{EFF}}$

To obtain the $\mathcal{L}_{\mathrm{eff}}$ value for each experimental setup we take the following steps. First, apply a set of cuts to reduce uninteresting events such as noise events, gamma ray scatters, neutron inelastic scatters and multiple elastic scatters. Next, the energy spectrum is obtained based on the light yield measurements and fitted to a spectrum predicted through Monte Carlo simulation. The following subsections explain these steps.
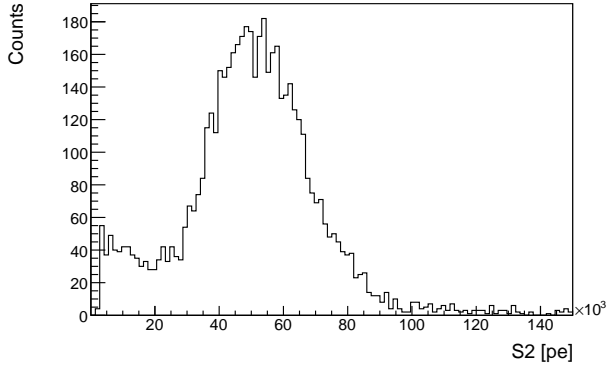
FIG. 6: $S2$ spectrum for 122 keV gamma rays in the dual phase detector.

A. Data Analysis

To remove uninteresting events two sets of cuts were used. The first set removes noise events and events outside the energy window of interest. The second set consists of two cuts used to select single elastic nuclear recoil events (Figure 7):

- The first cut is based on the pulse shape discrimination (PSD) of the organic scintillator. The PSD is based on the relation between pulse height and pulse area. This is an effective way to separate the neutron events from gamma events in the organic scintillator.

- The second cut uses the fact that neutrons take a longer time to travel from the LXe detector to the organic scintillator than gamma rays. The cut uses the time of flight (ToF) to remove events triggered by gamma rays or accidental coincidence. The cut selects the first half of the ToF peak because the contribution from scatters other than single elastic ones is negligible, as determined from Monte Carlo simulations.

The nuclear recoil energy distributions ($S1$ signals) after these two cuts are shown in Figures 8 **(a)** and **(b)** for 6 keV$_r$ nuclear recoils at zero electric field and 66 keV$_r$ nuclear recoils at 1.5 kV/cm, respectively. Similarly, Figures 8 **(c)** and **(d)** show $S2$ distributions for 6 keV$_r$ nuclear recoils at zero electric field and 66 keV$_r$ nuclear recoils at 1.5 kV/cm, after the cuts. In the 56 and 66 keV$_r$ runs it is easy to separate the background tail from the single elastic signal, as shown in Figure 8 **(b)**. This tail has been removed ($S1 < 50$ pe) to generate the $S2$ spectrum in Figure 8 **(d)**, and to find the $\mathcal{L}_{eff}$ values.
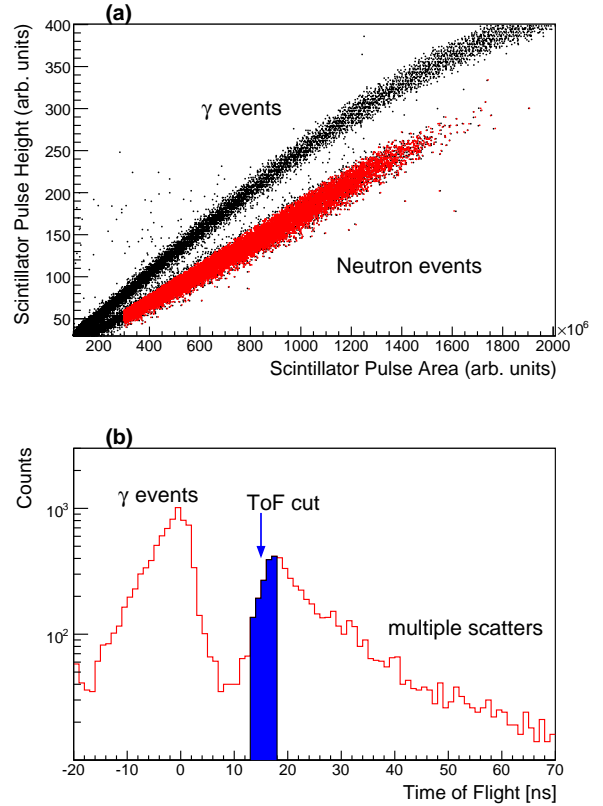

FIG. 7: (Color online) Two cuts used in the analysis to select single scatter nuclear recoil events. **(a)** pulse shape discrimination in the organic scintillator. **(b)** neutron time of flight between the LXe and the organic scintillator. Both plots show experimental data for 56 keV$_r$ run.

B. Monte Carlo simulation

The detector's response to neutrons is modeled using a Geant4 [17] simulation that takes into account the realistic setup of the experimental apparatus as described in Section II, including the water shield around the neutron generator, the polyethylene shield around the organic scintillator detector, the aluminum cryostat, the stainless steel cell, PTFE structure, PMTs, grids and LXe in the detector. The simulation stores the neutron scattering position, time, energy and type of events that deposit energy in both the LXe detector and the liquid scintillator.

For the simulations we follow the work by [12] and used the Xe(n,n)Xe scattering cross-sections from the updated ENDF/B-VII data, instead of the ENDF/B-VI cross-section used by default with the software. As discussed in [18], a ±3% uncertainty associated to the well depth parameter in the Optical Model Potential used to calculate the elastic cross-sections, leads to a conservative uncertainty which translates into an uncertainty up to ±3% in the nuclear recoil spectra. The latter is included
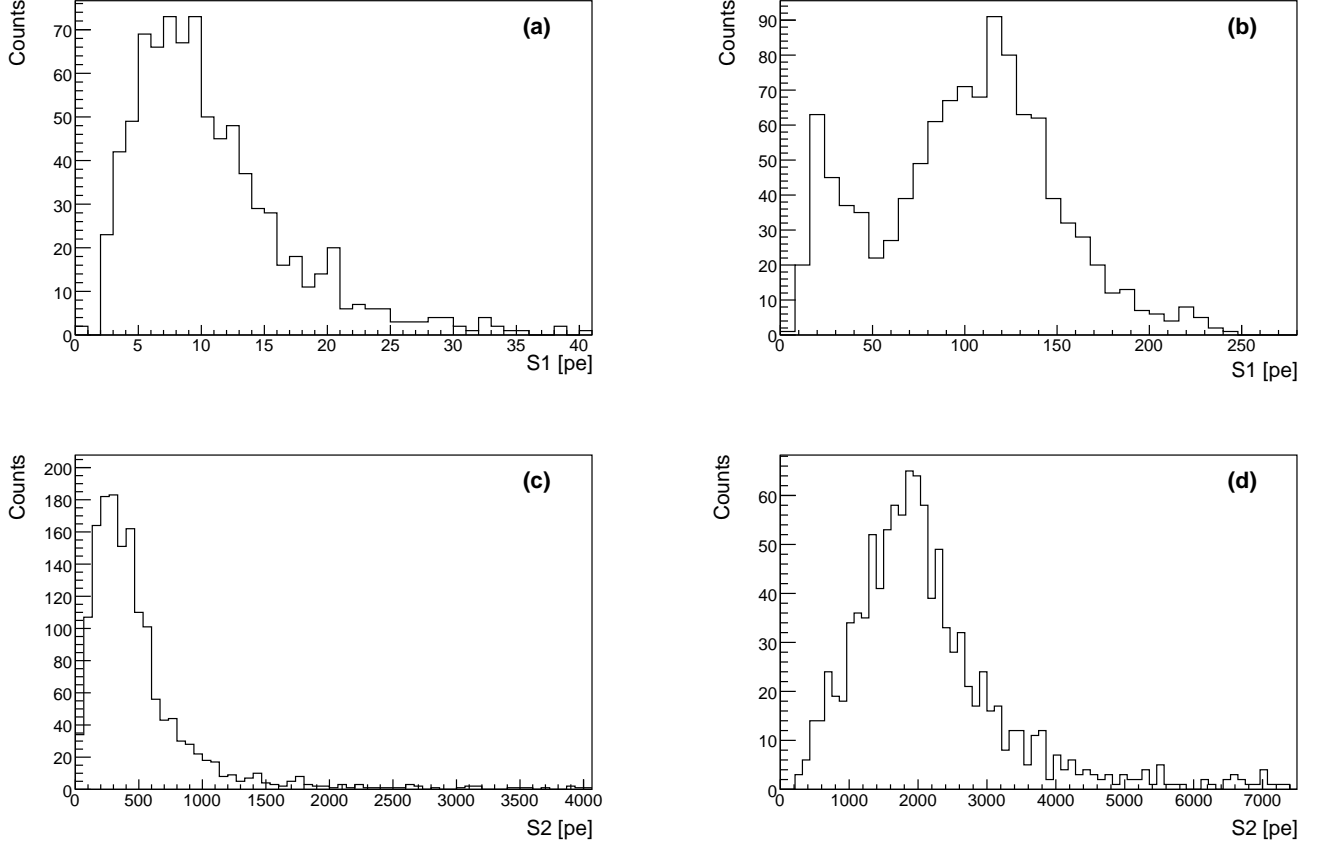
FIG. 8: $S1$ spectra in pe for **(a):** 6 keV$_r$ nuclear recoils at zero electric field and **(b):** 66 keV$_r$ nuclear recoils at 1.5 kV/cm, after applying the cuts. $S2$ spectra in pe for **(c):** 6 keV$_r$ nuclear recoils at zero electric field and **(d):** 66 keV$_r$ nuclear recoils at 1.5 kV/cm.

when calculating the $\mathcal{L}_{eff}$ systematic uncertainty.

Neutrons can deposit energy in LXe via elastic scattering, inelastic scattering, or a mixture of both. For most of the events that satisfy the ToF cut between the LXe and the liquid scintillator, neutrons come directly from the neutron generator, make a pure single elastic scatter in LXe and reach the liquid scintillator. Single elastic events give a peak (see Figure 9) at the energy E_r determined by the kinematics according to:

$$E_r \approx E_n \frac{2 m_n m_{Xe}}{(m_n + m_{Xe})^2}(1 - \cos\theta) \qquad (2)$$

where E_n is the incoming neutron energy (2.8 MeV), while m_n and m_{Xe} are the masses of the neutron and the Xe nucleus, and θ is the scattering angle. The spread of the energy deposition peak is from the spread of θ due to the geometric width of the LXe detector, the width of the organic scintillator and the distance between them.

Some of the neutrons from the generator may scatter first in other materials (e.g. PTFE) before entering the LXe detector. Neutrons may also scatter more than once in the LXe detector. These "multiple-scattering" events have a variety of scattering angles and, therefore, deposit a wider range of energies than the single elastic

scatters. This contributes to the background tail under the pure single scattering peak. Through minimization of non-active material, the geometry of the detector was designed to reduce background from multiple scattering events, especially for runs performed at low scattering angles. Inelastic scattering events are very few and make negligible contribution to the energy spectrum (less than 1%). A detailed description of the contributions of each background for each energy tested can be found in [19].

Although the LXe detector gives a high scintillation yield, detecting and resolving the peak for low energy nuclear recoils is still challenging. The energy spread for nuclear recoils below 10 keV$_r$ is dominated by statistical fluctuation of the photoelectrons in the PMTs. The trigger threshold, the trigger efficiency and the $S1$-finding algorithm efficiency must be taken into account in the analysis since not all events are effectively detected. In our measurement, the trigger of the LXe signal is from coincidence of the two PMTs with leading-edge discriminators. Effects of the trigger and software efficiencies are included in the Monte Carlo spectrum. A realistic model of the trigger efficiency was determined by a Monte Carlo simulation that included photon distribution into the two PMTs, quantum efficiencies, statistical
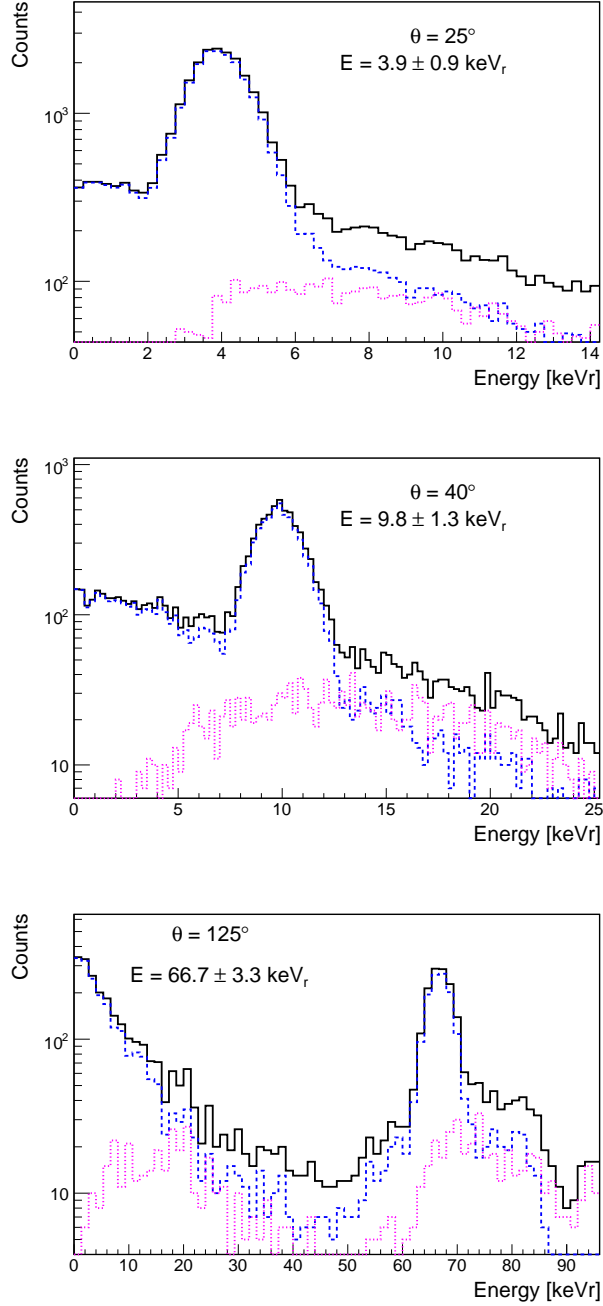
FIG. 9: (Color online) Simulated distribution of energy deposition in the LXe for 2.8 MeV neutrons that scatter and are tagged by the organic scintillator, for three different angles, assuming the same ToF cuts that were used in the experimental data. The solid line corresponds to all types of events, the blue dashed line to single elastic nuclear recoils, and the purple dotted line to multiple elastic scatters. Multiple scatter events and inelastic events are negligible compared to the single scatter events. The energy and uncertainty values indicated in the figure legends are based on the mean and variance (one sigma) of the peak for all events.

sampling of typical noise and single photoelectron waveforms in the PMTs, the electronic trigger thresholds, and the $S1$-finding algorithm in the analysis software. Figure 10 shows the overall trigger efficiency when combining these effects.
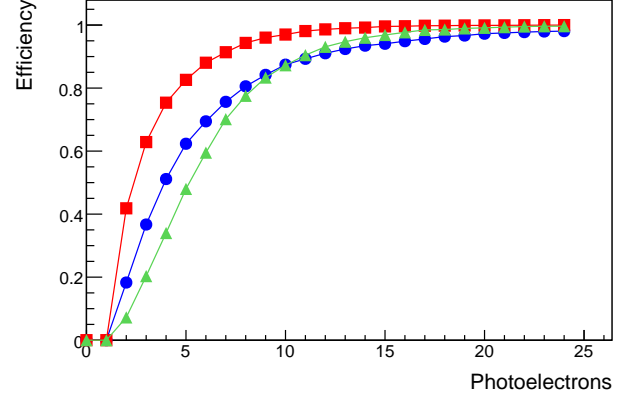

FIG. 10: (Color online) Detector triggering and software efficiencies for the single (▲) and dual phase (●) runs. The ■ points show the ideal case when the PMTs and the software have 100% efficiency for a single photoelectron.

For each energy studied, the $\mathcal{L}_{\mathrm{eff}}$ value is found by comparing the Monte Carlo generated spectrum with the measured spectrum, using a χ^2 test according to equation [20]:

$$\chi^2 = \sum_{i=1}^{N} \frac{(n_i - \nu_i)^2}{\nu_i} \qquad (3)$$

where N is the total number of bins, while n_i and ν_i are the measured and Monte Carlo generated number of events in each energy bin. To perform the χ^2 test, the total number of events in the Monte Carlo spectrum was normalized to that of the measured spectrum. The energy distribution (or ν_i at different energy bins) from the Monte Carlo spectrum varies with different input of $\mathcal{L}_{\mathrm{eff}}$ values. The best-fit $\mathcal{L}_{\mathrm{eff}}$ value is obtained by minimizing the χ^2 parameter. Figures 11 **(a)** and **(b)** show the data (points with error bars) and the Monte Carlo spectrum (line) after minimization, for 6 keV$_\mathrm{r}$ nuclear recoils at zero electric field and 66 keV$_\mathrm{r}$ nuclear recoils at 1.5 kV/cm. These plots correspond to the $S1$ spectra shown in Figures 8 **(a)** and **(b)**. Figures 11 **(c)** and **(d)** show the χ^2 vs. $\mathcal{L}_{\mathrm{eff}}$ histograms.

IV. RESULTS

The largest uncertainties in $\mathcal{L}_{\mathrm{eff}}$ derive from the χ^2 analysis and from the energy resolution applied to the Monte Carlo spectrum. The energy resolution is a combination of Poisson fluctuations in the PMTs, the PMT
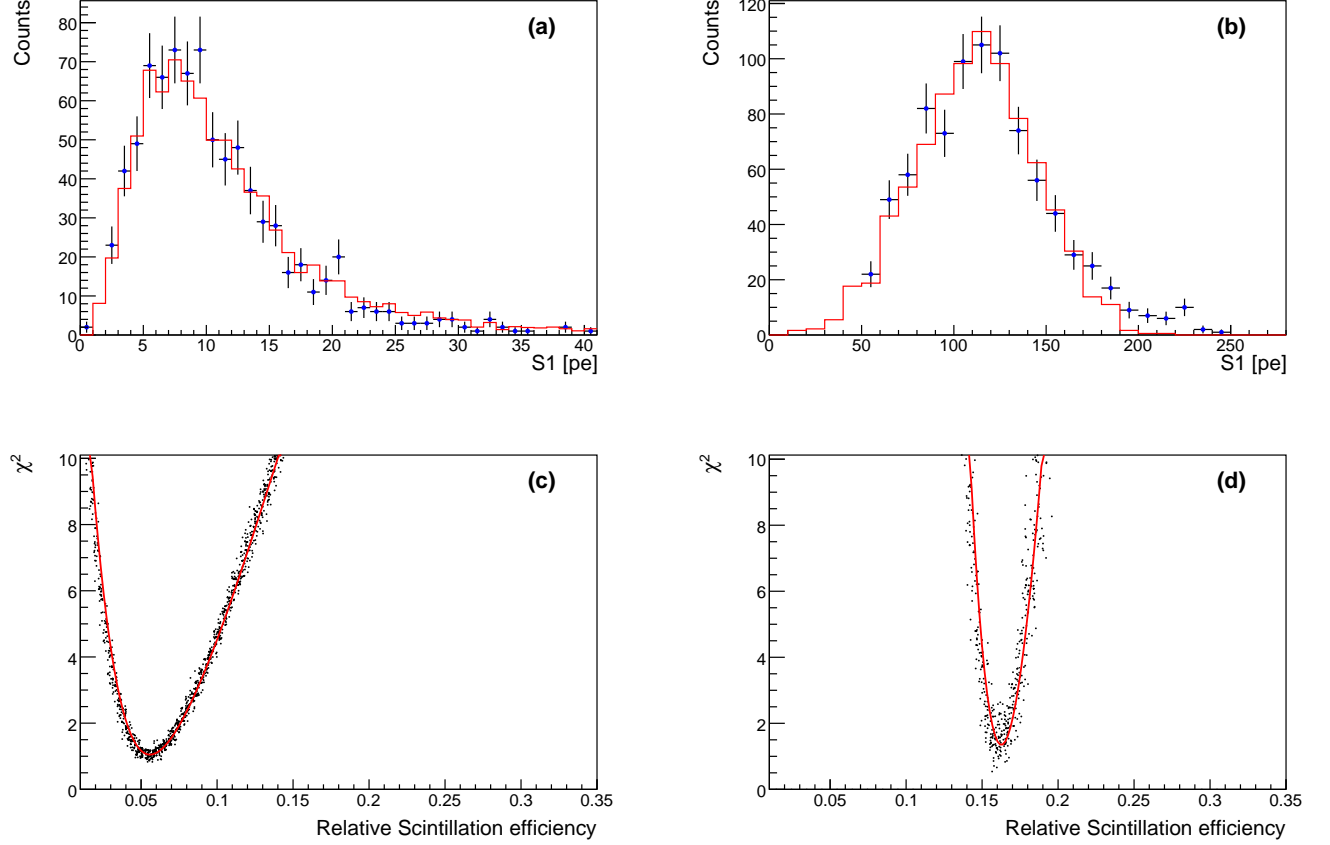
FIG. 11: (Color online) $S1$ measured spectrum (data points) and Monte Carlo comparisons (solid line) for **(a)** 6 keV$_r$ nuclear recoils at zero electric field and **(b)** 66 keV$_r$ nuclear recoils at 1.5 kV/cm. The background tail ($S1 < 50$ pe) for the 66 keV$_r$ run has been removed for the χ^2 test. Also shown are the χ^2 vs $\mathcal{L}_{eff}$ histograms for **(c)** 6 keV$_r$ nuclear recoil at zero electric field and **(d)** 66 keV$_r$ nuclear recoils at 1.5 kV/cm. The points show the different $\mathcal{L}_{eff}$ values tested while the curve is a fit to the points used to find the 1σ errors on the $\mathcal{L}_{eff}$ value.

gain fluctuations, the geometry of the cell (σ_{geo}), the optical properties of the materials and the intrinsic resolution of the LXe. The total energy resolution, σ, defined as the root mean squared of the terms mentioned, was measured to be $\sigma = (3.2 \pm 0.4)\sqrt{N}$ with N the number of photoelectrons for 56 and 66 keV$_r$. This relationship was assumed for determining all $\mathcal{L}_{eff}$ values. Because the geometry resolution is already included in the simulation, the Monte Carlo data were convolved using an energy resolution $\sigma' \equiv \sqrt{\sigma^2 - \sigma_{geo}^2}$. The gain fluctuations were measured from the calibration runs, while the error due to the optical properties was determined from an independent light simulation. After subtracting the geometry resolution, the overall uncertainty on σ' is estimated to be $\pm 1.0\sqrt{N}$, and this is propagated through to compute the systematic uncertainty in $\mathcal{L}_{eff}$. The total errors are shown in Figure 12 and given in Table I. Figures 12 and 13 compare our $\mathcal{L}_{eff}$ results with previous analyses. Since the data show no significant nuclear quenching due to the electric field, $\mathcal{L}_{eff}$ is computed

using data from all of the different runs, regardless of electric field.

An electric field applied to LXe will suppress electron-ion recombination and thus reduce the scintillation yield. This field induced quenching is significant for electronic recoils. For example, at 1 kV/cm, scintillation light yield from 122 keV gamma rays in LXe is reduced to 53% of its value at zero field [7]. For nuclear recoils, a near-unity value of S_n has been measured at 56 keV$_r$[7, 10]. Here we measured the field induced quenching for nuclear recoils as low in energy as 4 keV$_r$. No significant field quenching was observed for any energy or electric field. The average field induced quenching factor, S_n, for 56 keV$_r$ nuclear recoils at an electric field of 0.73 kV/cm is about 95% as given in Table I.

From the dual phase data we can determine the ionization yield (number of electrons escaping recombination per unit recoil energy). This number is determined from the $S2$ peak position for the nuclear recoils (Figure 8**(d)** for example) and the number of photoelectrons per electron determined from the ^{57}Co calibration runs. Figure
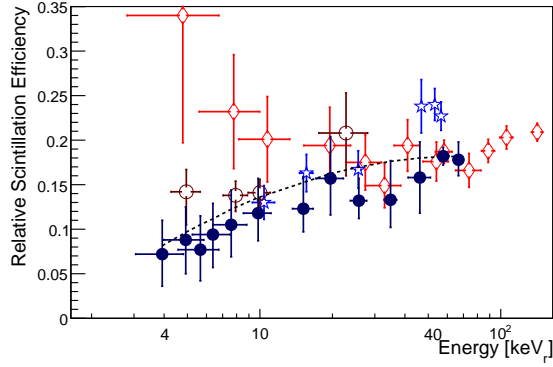
FIG. 12: (Color online) Scintillation efficiency for nuclear recoils relative to that of 122 keV gamma rays in LXe at zero field, comparing this work (●) to previous measurements from Arneodo (△) [5], Akimov (□) [6], Aprile (☆) [7], Chepel (◇) [8] and Aprile (○)[9]. Also shown is the theoretical model (dashed line) explained in Section V, which includes the Lindhard factor, an electronic quenching due to bi-excitonic collisions and the effect of escaping electrons.
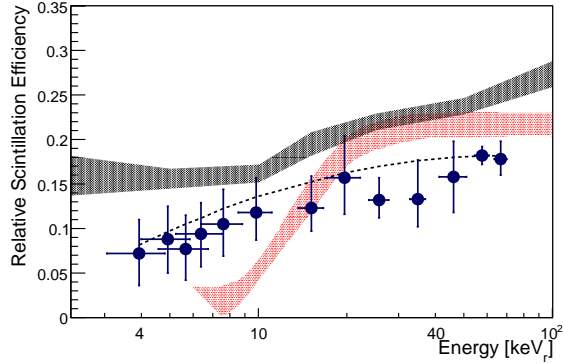

FIG. 13: (Color online) Scintillation efficiency for nuclear recoils measured in this work (●) and the theoretical model (dashed line) compared to the scintillation efficiency found from the neutron calibration data by the XENON10 (top shaded area) [12] and the ZEPLIN-III (bottom shaded area) [4] collaborations.

14 shows the energy dependence of the ionization yield measured in this work for 1.0 kV/cm and 4.0 kV/cm, as well as previous measurements [10] and the calculated values when comparing the XENON10 nuclear recoil data and Monte Carlo simulations [12]. The ionization yield errors shown in Figure 14 were derived from the width of the $S2$ signals from nuclear recoils and from the ^{57}Co calibrations. By comparing the dual phase runs triggered by the $S1$ signals with the runs triggered by the $S2$ signals, we determined that there is no significant uncertainty in the $S2$ signals due to the trigger.
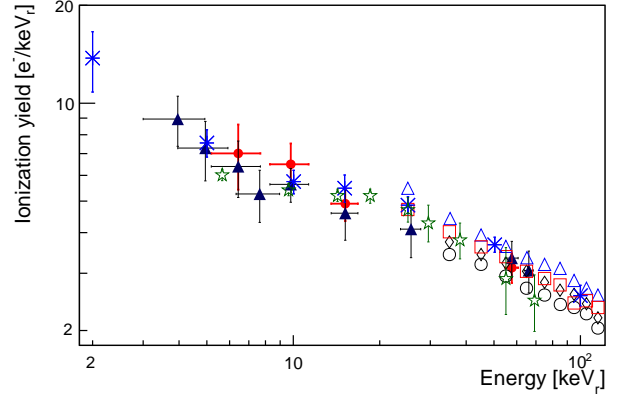

FIG. 14: (Color online) Ionization yield as a function of recoil energy. Shown are the measured values in this work at 1.00 kV/cm (▲) and 4.00 kV/cm (●), along with previously measured values at 0.10 kV/cm (○), 0.27 kV/cm (□), 2.00 kV/cm (△) and 2.30 kV/cm(◇) from [10], error bars omitted for clarity. Also shown are the ionization yields calculated by comparing the XENON10 nuclear recoil data and the Monte Carlo simulations [12] for single elastic recoils at 0.73 kV/cm, using two different methods (✳ and ☆).

V. EMPIRICAL MODEL OF $\mathcal{L}_{\text{EFF}}$

The data shown above reveal a relative scintillation efficiency that decreases with decreasing energy. A suitable theoretical expression for $\mathcal{L}_{\text{eff}}$ in LXe can be written as the product of at least three components:

$$\mathcal{L}_{\text{eff}} = q_{\text{ncl}} \cdot q_{\text{esc}} \cdot q_{\text{el}} \tag{4}$$

First is the Lindhard factor [21], q_{ncl}, which quantifies the larger fraction of energy dissipated into atomic motion or heat in a nuclear recoil compared to that for an electron recoil. As a function of recoil energy, E_r, the Lindhard factor can be written as

$$q_{\text{ncl}} = \frac{k \cdot g(\varepsilon)}{1 + k \cdot g(\varepsilon)} \tag{5}$$

where for a nucleus with atomic number Z and mass number A, $k = 0.133 \cdot Z^{2/3} \cdot A^{-1/2}$, $g(\varepsilon) = 3.0\varepsilon^{0.15} + 0.7\varepsilon^{0.6} + \varepsilon$, where ε is the reduced energy $\varepsilon = 11.5 \cdot E_r \cdot Z^{-7/3}$.

The second term, q_{esc}, is the reduction of the scintillation light yield due to *escaping electrons*. These are electrons produced by ionization that thermalize outside the Onsager radius and become free from recombination even in the absence of an electric field [22]. The effect of escaping electrons has been observed for electron recoils [22] and has only recently been considered as a possible additional factor governing the total scintillation reduction for nuclear recoils in LXe [23]. This is because of the surprisingly high ionization yield from nuclear recoils [10]. This factor can be expressed in terms of the ratio

TABLE I: $\mathcal{L}_{\text{eff}}$ and S_n values for the different nuclear recoil energies studied. The third column gives the $\mathcal{L}_{\text{eff}}$ values relative to 122 keV gamma rays. The first error is the statistical uncertainty, and the second error is the systematic uncertainty.

θ	E_r [keV$_r$]	$\mathcal{L}_{\text{eff}}$ at 0.0 kV/cm	S_n 0.73 kV/cm	S_n 1.0 kV/cm	S_n 1.5 kV/cm	S_n 4.0 kV/cm
125	66.7 ± 3.3	$0.178\,^{+0.018+0.010}_{-0.016-0.009}$	0.91 ± 0.07	1.11 ± 0.09	0.88 ± 0.06	-
110	57.7 ± 3.2	$0.182\,^{+0.009+0.004}_{-0.009-0.002}$	0.95 ± 0.05	0.95 ± 0.06	0.93 ± 0.04	0.93 ± 0.06
95	46.1 ± 4.9	$0.158\,^{+0.038+0.010}_{-0.039-0.009}$	0.97 ± 0.08	-	0.82 ± 0.08	-
80	34.9 ± 2.1	$0.133\,^{+0.042+0.014}_{-0.029-0.012}$	1.33 ± 0.26	-	1.30 ± 0.25	-
67	25.7 ± 2.0	$0.132\,^{+0.025+0.001}_{-0.019-0.006}$	0.95 ± 0.06	0.91 ± 0.12	0.95 ± 0.07	-
58	19.6 ± 2.6	$0.157\,^{+0.046+0.008}_{-0.036-0.019}$	0.70 ± 0.06	-	1.03 ± 0.13	-
50	15.1 ± 1.5	$0.123\,^{+0.030+0.019}_{-0.023-0.014}$	0.83 ± 0.16	1.02 ± 0.20	1.01 ± 0.15	1.08 ± 0.18
40	9.8 ± 1.3	$0.118\,^{+0.027+0.029}_{-0.022-0.022}$	0.91 ± 0.17	1.64 ± 0.50	0.98 ± 0.18	1.62 ± 0.45
35	7.6 ± 1.2	$0.105\,^{+0.028+0.026}_{-0.022-0.029}$	0.79 ± 0.28	1.06 ± 0.30	0.79 ± 0.28	-
32	6.4 ± 1.1	$0.094\,^{+0.027+0.023}_{-0.022-0.029}$	0.92 ± 0.37	1.25 ± 0.45	0.93 ± 0.38	1.38 ± 0.52
30	5.7 ± 1.1	$0.077\,^{+0.028+0.027}_{-0.022-0.026}$	1.35 ± 0.67	-	1.18 ± 0.61	-
28	4.9 ± 0.9	$0.088\,^{+0.026+0.026}_{-0.023-0.032}$	1.16 ± 0.45	1.34 ± 0.50	0.87 ± 0.35	-
25	3.9 ± 0.9	$0.073\,^{+0.034+0.018}_{-0.025-0.026}$	1.19 ± 0.52	1.30 ± 0.38	1.88 ± 0.78	-

between the initial number of excitons and electron-ion pairs $\alpha \equiv N_{\text{ex}}/N_i$, and the fraction of escape electrons over the total electron-ion pairs $\beta \equiv N_{\text{esc}}/N_i$.

$$q_{\text{esc}} = \frac{N_{\text{ex}} + N_i - N_{\text{esc}}}{N_{\text{ex}} + N_i - N_{\text{esc}}^{122}} = \frac{\alpha + 1 - \beta_{\text{NR}}}{\alpha + 1 - \beta^{122}} \qquad (6)$$

For this work we select $\alpha = 0.06$, measured for electron recoils in LXe [22, 24]. β^{122} is the fraction of escaping electrons for 122 keV electron recoils in LXe and is calculated to be 0.31 based on the ^{57}Co data from [10] and the method described in [22]. β_{NR} can be calculated based on the nuclear recoil ionization yield reported in [10] and those measured in this work (Figure 14). The β_{NR} values estimated for the different energies studied in this work are given in Figure 15.

The last term in the $\mathcal{L}_{\text{eff}}$ model is the scintillation light quenched by bi-excitonic collisions, q_{el}, as proposed by Hitachi [25] to explain the much lower measured $\mathcal{L}_{\text{eff}}$ values than are predicted by q_{ncl} alone. Bi-excitonic collisions have the effect of two excitons producing a single photon instead of two photons. A recent paper [26] extends the study of quenching due to bi-excitonic collision by including the varying quenching due to different stopping power for different energy recoils, as quantified by Birks' Law [27]. Thus,

$$q_{\text{el}} = \frac{1}{1 + k_B \cdot \frac{dE}{dx}} \qquad (7)$$

We obtain dE/dx values from SRIM [28] and fit the k_B parameter to match our $\mathcal{L}_{\text{eff}}$ model to the data at 56 keV$_r$, finding $q_{\text{el}} = 0.65$. Hitachi [25] used $q_{\text{el}} = 0.68$ to match his model and the data at 60 keV$_r$.
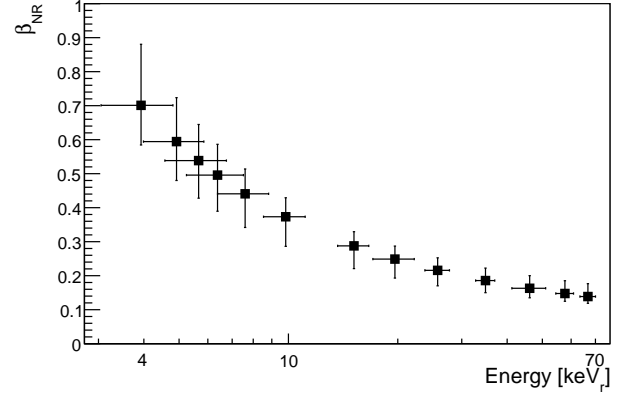

FIG. 15: Fraction of escape electrons for nuclear recoils, β_{NR}, as a function of recoil energy used in this work.

VI. DISCUSSION

The high energy points (56 and 66 keV$_r$) agree with previous $\mathcal{L}_{\text{eff}}$ measurements. The $\mathcal{L}_{\text{eff}}$ measurements from 20 to 46 keV$_r$ suffer from a low differential neutron-nuclear elastic scattering cross-section compared to lower nuclear recoil energies and thus have higher backgrounds. Therefore, this results in larger statistical errors for measurements in this energy range. The detector was designed to minimize multiple scattering background for energies below 15 keV$_r$ (see Figure 9). For 10 keV$_r$, the $\mathcal{L}_{\text{eff}}$ value agrees with previous experiments. For energies below 10 keV$_r$, our results

are lower than the Chepel [8] results and agree with the Aprile [9] values within errors. However, our results suggest a decreasing $\mathcal{L}_{\text{eff}}$ with decreasing energy and not a constant as suggested by [12]. Our results disagree with the $\mathcal{L}_{\text{eff}}$ curves found by comparing calibration data and Monte Carlo simulations (Figure 13) done by the XENON10 [12] and ZEPLIN-III [4] collaborations. The ionization yield (Figure 14) measured in this work is in agreement with previous measurements [10] and the XENON10 Monte Carlo analysis [12].

The theoretical $\mathcal{L}_{\text{eff}}$ models by Lindhard [21] and Hitachi [25] fail to explain our measurements. The theoretical model presented in this paper, which includes the effect of escape electrons, fits our measurements within errors. This $\mathcal{L}_{\text{eff}}$ model is a simple one and several corrections can be done. As pointed out in [29], for LXe the Lindhard model is a crude approximation below 15 keV_{r}, and so the model could be improved below this energy. A more general expression for q_{esc} could also be used that includes different values of α for nuclear recoils and electron recoils [24] as well as any energy dependence of α.

The $\mathcal{L}_{\text{eff}}$ energy dependence measured in this work affects the dark matter limits set by LXe detectors. Figure 16 shows the XENON10 result [3] (top solid line) found using $\mathcal{L}_{\text{eff}}$=0.19, as well as the projected spin-independent limits using $\mathcal{L}_{\text{eff}}$=0.19 (solid blue line) and the $\mathcal{L}_{\text{eff}}$ from this work (dotted line). The latter two curves are 90% confidence limits based on Feldman-Cousins unified approach [30] for a LXe detector with a 30,000 kg day exposure with no backgrounds in the 0.95 to 5.7 keVee energy window. This energy window corresponds to 5 to 30 keV_{r} using $\mathcal{L}_{\text{eff}}$=0.19, and to 8.4 to 39.0 keV_{r} using the measured $\mathcal{L}_{\text{eff}}$ in this work. At a WIMP mass of 10 GeV/c^2, the WIMP nucleon cross-section limit is more than an order of magnitude higher with the measured $\mathcal{L}_{\text{eff}}$, compared to the limit found assuming $\mathcal{L}_{\text{eff}}$=0.19. At 50 GeV/c^2 the WIMP nucleon cross-section limit is only 35% higher and is 20% higher above 100 GeV/c^2.
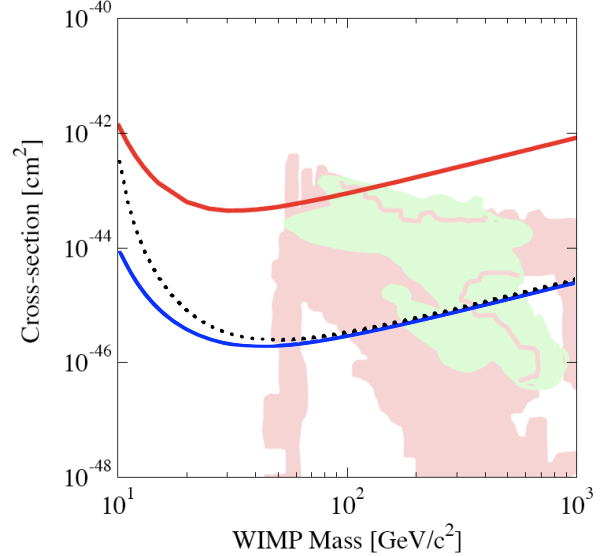

FIG. 16: (Color online) Projected spin independent dark matter limits for a LXe detector with 30,000 kg day exposure and 0.95 to 5.7 keVee energy window. The bottom solid line shows the limit with $\mathcal{L}_{\text{eff}}$=0.19 (5 to 30 keV_{r} window) while the dotted line shows the limit calculated with the measured $\mathcal{L}_{\text{eff}}$ (8.4 to 39.0 keV_{r} window). Also plotted are the XENON10 result [3] (top solid line) and the regions predicted by [31] (red shaded region) and [32] (green shaded region). Plot generated using [33].

collisions and escape electrons that agrees with our results. Our $\mathcal{L}_{\text{eff}}$ results and model suggest a decreasing $\mathcal{L}_{\text{eff}}$ with decreasing energy. This result changes the spin independent limit as shown in Figure 16. Although our $\mathcal{L}_{\text{eff}}$ result significantly changes the cross-section limit at low WIMP masses, the limit is only changed by 20% for WIMP masses above 100 GeV/c^2.

In addition, we present the results for the nuclear recoil ionization yield and calculated the fraction of escape electrons for nuclear recoil energies between 4 and 66 keV_{r}.

VII. SUMMARY

This work presents a new $\mathcal{L}_{\text{eff}}$ measurement for energies between 4 and 66 keV_{r}. This measurement was done using a single phase ($S1$ signal only) and a dual phase detector ($S1$ and $S2$ signals) to understand the detector's response at low energies. Each energy measured was repeated with at least three different electric fields finding no clear dependence of nuclear recoil scintillation yield at low energies. We also present a theoretical $\mathcal{L}_{\text{eff}}$ model including nuclear quenching, bi-excitonic

[1] G. Jungman, M. Kamionkowski, and K. Griest, Phys. Rep. **267**, 195 (1996).

[2] G. Alner *et al.*, Astropart. Phys. **28**, 287 (2007).

[3] J. Angle *et al.*, Phys. Rev. Lett. **100**, 021303 (2008).

[4] V. Lebedenko *et al.*, arXiv **0812.1150** (2008).

[5] F. Arneodo *et al.*, Nucl. Inst. and Meth. A **449**, 147 (2000).

[6] D. Akimov *et al.*, Phys. Lett. B **524** (2002).

[7] E. Aprile *et al.*, Phys. Rev. D. **72** (2005).

[8] V. Chepel *et al.*, Astropart. Phys. **26**, 58 (2006).

[9] E. Aprile *et al.*, Phys. Rev. C **79**, 045807 (2009).

[10] E. Aprile *et al.*, Phys. Rev. Lett. **97** (2006).

[11] P. Sorensen, *A position-sensitive liquid xenon time projection chamber for direct detection of dark matter: the Xenon10 experiment*, PhD thesis, Brown University, 2008.

[12] P. Sorensen *et al.*, Nucl. Inst. and Meth. A **601**, 339 (2009).

[13] D. Chichester, J. Simpson, and M. Lemchak, J. Radioanal. Nucl. Chem. **271**, 629 (2007).

[14] W. Lippincott *et al.*, Phys. Rev. C **78**, 035801 (2008).

[15] J. Nikkel, R. Hasty, W. Lippincott, and D. McKinsey, Astropart. Phys. **29**, 161 (2008).

[16] K. Ni *et al.*, Nucl. Inst. and Meth. A **582**, 569 (2007).

[17] S. Agostinelli and et al, Nucl. Inst. and Meth. B **506**, 250 (2003).

[18] M. Pignil, M. Herman, P. Oblozinsky, and D. Rochman, Brookhaven National Laboratory Report No. BNL-79261-2007-IR, 2007 (unpublished).

[19] A. Manzur, *Relative scintillation efficiency of liquid xenon in the XENON10 direct dark matter search*, PhD thesis, Yale University, 2009.

[20] W. M. Yao *et al.* [Particle Data Group], J. Phys. G **33**, 1 (2006).

[21] J. Linhard, M. Scharff, and P. Thomsen, Mat. Fys. Medd. Dan. Vid. Selsk **33** (1963).

[22] T. Doke, A. Hitachi, J. Kikuchi, and K. Masuda, Jpn. J. Appl. Phys. **41**, 1538 (2002).

[23] T. Shutt, Private communication (2007).

[24] C. Dahl, *The physics of background discrimination in liquid xenon, and the first results from XENON10 in the hunt for WIMP dark matter*, PhD thesis, Princeton University, 2009.

[25] A. Hitachi, Astropart. Phys. **24**, 247 (2005).

[26] D.-M. Mei, Z.-B. Yin, L. Stonehill, and A. Hime, Astropart. Phys. **30**, 12 (2008).

[27] J. Birks and F. Black, Proc. Phys. Soc. A **64**, 511 (1951).

[28] SRIM, Particle interactions with matter, 2009.

[29] A. Hitachi, J. Phys: Conf. Ser. **65** (2007).

[30] G. Feldman and R. Cousins, Phys. Rev. D. **57**, 3873 (1998).

[31] E. Baltz and P. Gondolo, JHEP **10**, 052 (2004).

[32] R. Trotta, F. Feroz, M. Hobson, L. Roszkowski, and R. Ruiz-de Austri, JHEP **12**, 024 (2008).

[33] DMTOOLS, http://dmtools.brown.edu, http://dmtools.berkeley.edu, 2009.